Equation Chapter 1 Section 1PROCEEDINGS, Thirty-Fifth Workshop on Geothermal Reservoir Engineering
Stanford University, Stanford, California, February 1-3, 2010
SGP-TR-188

STUDY AND SIMULATION OF TRACER AND THERMAL TRANSPORT IN FRACTURED RESERVOIRS

Egill Juliusson and Roland N. Horne

Stanford University
367 Panama Street
Stanford, CA, 94305, USA
e-mail: egillj@stanford.edu

ABSTRACT

This paper discusses a simulation study of tracer and thermal transport in fractured geothermal reservoirs. The motivation was to explore the relationship between tracer returns and thermal breakthrough in production wells.

By employing the discrete fracture discretization method introduced by Karimi-Fard et al. (2003), we were able to run simulations with fracture grid blocks of realistic dimension. This enabled us to obtain relatively realistic models of tracer and thermal transport and investigate the sensitivity of the return profiles to various reservoir properties. Moreover, the visualization of changes in temperature, pressure and tracer concentration in the reservoir were useful to gain better insight into the behavior of these properties in the fractured systems.

The initial plan was to use the TOUGH2 code to do the simulations, but after running into a number of problems with the solver and time stepping it was decided to switch to the General Purpose Research Simulator (GPRS) developed at the Department of Energy Resources Engineering at Stanford University. The simulations were carried out using a two-dimensional thermal black-oil model, without gravity effects.

In short we found that a quantitative relationship between the tracer return profile and the thermal return profile is hard to formulate, even for relatively simple cases. The relationship will depend, for example, the flow rate through the fracture and the types of boundary conditions for the matrix surrounding the fracture. Moreover, the fracture distribution will be important, although in the case investigated here, the thermal profile was not as severely affected as anticipated.

INTRODUCTION

The motivation for this work was to investigate the extent to which tracer returns could be used to predict thermal breakthrough in production wells. This topic has previously been discussed e.g. by Bodvarsson & Pruess (1984), Urbino & Horne (1991), Sullera & Horne (2001) and Horne & Szucs (2007). This idea becomes particularly interesting with regards to optimization of reinjection scheduling, as discussed by Lovekin & Horne (1989). However, the tracer testing approach has some limitations since the returns from a tracer test will vary with changes in the reinjection schedule. Moreover, Pruess and Bodvarsson (1984) showed that in vertically fractured reservoirs the tracer signal will not suffice to fully characterize the thermal characteristics of the flow path. They state that the flow path characteristics can be determined more accurately using a mixed numerical/semi-analytical approach with the combined interpretation of pressure, temperature and tracer. These analyses show that understanding the combined transport of pressure, tracer and heat in fractured reservoirs is an essential but non-trivial task.

Simulation of tracer transport in fractured reservoirs is also a particularly challenging problem. One reason is that for the most commonly used discretization schemes the computations will be adversely affected if a saturation front is allowed to travel more than one gridblock per time step. This obviously causes problems in models with saturations travelling fast through extremely small gridblocks. Lately some intriguing advances have been made to (partially) solve this problem. An efficient simulation technique for tracer transport in fractured reservoirs, using a discrete fracture discretization was illustrated by Lange et al. (2005), where a double-upstream) discretization scheme was used to minimize numerical diffusion in a mass transport model. Wu and Forsyth (2008) added similar advancements (a flux-limiter scheme) for tracer dispersion to the TOUGH2 simulation code (which simulates mass and thermal transport). This particular update of the code is however not yet available to the public. With the approach of Wu et al. (2000, 2008) the explicit modeling of the fracture gridblocks is avoided by assigning a full tensor dispersion coefficient to relatively large gridblocks.

Combined simulation of tracer and thermal transport in explicitly modeled fractures has, to our knowledge, only been carried out using; a) simple Cartesian grids or; b) with two-dimensional models where the heat exchange with the fracture walls is approximated with a semi-analytical model for the cooling of the fracture walls, using the formulation of Vinsome & Westerveld (1980).

In this work we have utilized the method of Karimi-Fard et al. (2003) to discretize the permeability on an unstructured two-dimensional grid. This way the transport physics in the fracture network are captured more accurately, especially in sparsely fractured rock such as might be encountered in Enhanced Geothermal Systems (EGS). This simulation method is also interesting since it allows clear visualization of the propagation of the simulated properties (pressure, temperature, tracer saturation etc.) in time. However, with more densely fractured rock, this method quickly becomes infeasible because of the lack in computational efficiency. In such cases, an upscaling method could provide a practical alternative (e.g. Gong, 2007).

DISCRETE FRACTURE MODEL

This section describes briefly how the reservoir simulations were set up to simulate flow through fractured medium.

The first step in setting up the model was to generate a fracture network. A number of software packages are available for creating these, e.g. FRACMAN from Golder & Associates and FRACA from Beicip-Franlab. However, in order to keep the study simple, a two-dimensional network was created in MATLAB with a code loosely based on the geomechanical process of fracture formation. Further discussion on the code can be found in Juliusson and Horne (2009).

After the fracture network had been generated, a suitable computational grid had to be formed. This was accomplished using the open source mesh generator Triangle (Shewchuk, 1996). The program and all associated commands and files are well described on the Triangle website, http://www.cs.cmu.edu/~quake/triangle.html. Figure 1 shows a stochastic fracture network with a conforming triangular grid.

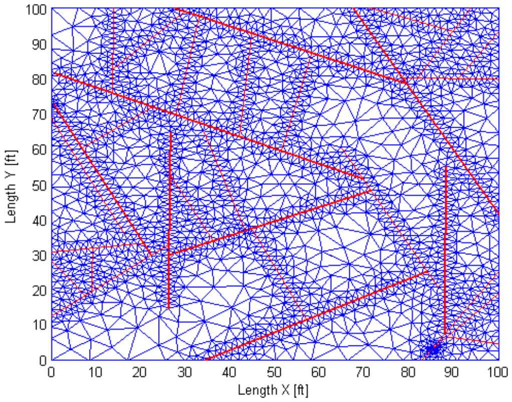

Figure 1: An example of a synthetic fracture network (red) and a mesh (blue) that conforms to the fractures. The width of the red lines is indicative of the width assigned to the fracture elements.

One of the major issues involved in modeling fractures explicitly in reservoir simulators relates to the intersection of the fractures. Handling this intersection in the "usual" manner leads to very small gridblocks (Figure 2) which can adversely affect the numerical stability and computational efficiency of the simulation.

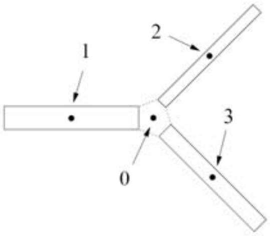

Figure 2: A very small gridblock (labeled 0) is formed at the intersection of fractures, on a computational grid where fractures are modeled discretely. Figure taken from Karimi-Fard et al. (2003).

By using the discretization scheme introduced by Karimi-Fard et al. (2003) the small gridblocks formed at fracture intersections were eliminated. The key element in their approach was to apply the star-delta transformation, which is more commonly used to solve problems in electrical engineering (Figure 3).

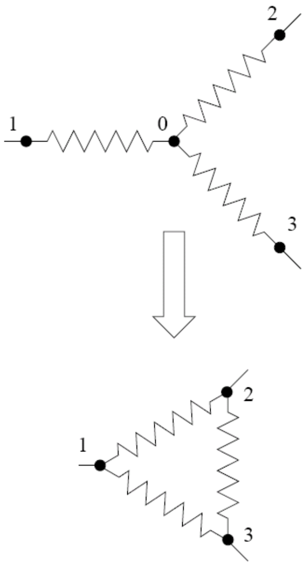

Figure 3: Intersections of multiple fractures can be converted to simpler connections using the star-delta transformation. Figure taken from Karimi-Fard et al. (2003).

From the star-delta transformation transmissibility between each connecting fracture element could be computed, using the formulation

$$T_{ij} = \frac{\alpha_i \alpha_j}{\sum_{k=1}^{n} \alpha_k} \tag{1}$$

where

$$\alpha_i = \frac{A_i k_i}{D_i} \tag{2}$$

and k denotes permeability, *A* is the cross sectional area at the fracture intersection and *D* is the distance from the centroid of the fracture block to the center of the fracture intersection.

Each fracture was assigned a width, *w*, and the corresponding permeability was determined by

$$k = \frac{w^2}{24} \tag{3}$$

For single phase flow, the transmissibility values are related to the flow between two adjoining elements, *i* and *j*, by

$$Q_{ij} = \frac{T_{ij}}{\mu_{ij}}(p_j - p_i) \tag{4}$$

where *Q* is the flow rate, *T* is the transmissibility, μ is dynamic viscosity and *p* is the pressure in the corresponding gridblock.

Our initial plan was to use the TOUGH2 code to carry out the required simulation work. However, TOUGH2 was not equipped to handle transmissibility terms as input data for individual connections. To account for that, the TOUGH2 code was modified such that it could take permeability values as input through the connection list (CONNE). To be exact, the last column of the connection list (which is meant to contain data for radiative heat transfer, SIGX) was used as the input column for connection-wise permeability values. These permeability values were calculated using the transmissibility formulation given by equation (1), and then dividing by a similar number but calculated with $k = 1$, i.e.

$$k_{ij} = \frac{\alpha_i \alpha_j}{\sum_{k=1}^{n} \alpha_k} \Bigg/ \frac{\beta_i \beta_j}{\sum_{k=1}^{n} \beta_k} \tag{5}$$

where

$$\beta_i = \frac{A_i}{D_i} \tag{6}$$

Then the values *D* and *A* could be supplied in the usual way through the connection list and the transmissibility was recalculated internally in TOUGH2. Note that the permeability values supplied in the ROCKS section and/or ELEME section of the TOUGH2 input file were all set to one, such that they would not interfere with the values supplied through the connection list (CONNE).

The modified version of TOUGH2 seemed to work well, in the sense that it yielded physically realistic output for the tracer returns. However, we ran into trouble when running the code for longer simulation times which would be required to observe thermal breakthrough times. We believe that the problem is related to the time stepping algorithm and/or simply the fact that the set of equations involved are too hard to solve for the solvers used by TOUGH2.

As an alternative we decided to use the Stanford General Purpose Reservoir Simulator (GPRS) (Cao, 2002; Voskov, 2006). All simulations with GPRS were run using the black-oil thermal module, where water was injected into a fully "oil" saturated reservoir, where the "oil" phase had all the equivalent properties of water. Capillary pressure was set to zero and X-curve relative permeability was used such that the two phases would interact as if there was only one phase. The pressure and temperature were set such that the reservoir fluid always remained as single phase liquid.

GOVERNING EQUATIONS

Before looking into simulations of specific fracture formations it was useful to review the governing equations of mass and energy rates for a unit volume, and see how much could be understood from employing some simplifying assumptions.

For single phase flow of κ components the mass equation can be written as (see notation in Table 1)

$$\begin{aligned}&\frac{\partial}{\partial t}(\varphi\rho^{\kappa}X^{\kappa})\\&=-\nabla\cdot\left(\frac{k\rho^{\kappa}\nabla p}{\mu^{\kappa}}X^{\kappa}+\varphi\rho^{\kappa}d^{\kappa}_{mol}\nabla X^{\kappa}\right)+q^{\kappa}\end{aligned}\tag{7}$$

The energy equation can be formulated as

$$\begin{aligned}&\frac{\partial}{\partial t}\left(\varphi\rho^{\kappa}X^{\kappa}u^{\kappa}+(1-\varphi)\rho_R u_R\right)\\&=-\nabla\cdot\left(\frac{k\rho^{\kappa}\nabla p}{\mu^{\kappa}}X^{\kappa}h^{\kappa}+\lambda\nabla T\right)+w^{\kappa}\end{aligned}\tag{8}$$

Table 1: Notation used for governing equations.

φ	Porosity
ρ	Density (kg/m^3)
X	Mass fraction of component
κ	Superscript that denotes component (water or tracer)
t	Time (sec)
k	Absolute permeability (m^2)
p	Pressure (Pa)
μ	Dynamic viscosity (Pa-s)
d	Molecular diffusion coefficient (m^2/s)
q	Mass source/sink (kg/s-m^3)
u	Specific internal energy (J/kg)
R	Subscript that denotes rock
T	Temperature (C)
h	Specific enthalpy (J/kg)
λ	Thermal conductivity (W/m-C)
w	Energy source/sink (W/m^3)
y	Distance (m)
c	Specific heat capacity (J/kg-C)
V	Subscript referring to volume

In most of the cases we considered the matrix permeability was much smaller than that of the fracture, and therefore the derivative along the fracture (here y direction) would dominate. Given that molecular diffusion is on the order of 10^{-10} for liquid tracers, we assumed that this could be discarded. For the temperature/pressure range observed, the density changes could be considered negligible over incremental distances in time and space. Therefore the mass balance equation could practically be reduced to

$$\varphi\frac{\partial}{\partial t}(X^{\kappa})=-\frac{d}{dy}\left(\frac{kX^{\kappa}}{\mu^{\kappa}}\frac{dp}{dy}\right)+\frac{q^{\kappa}}{\rho^{\kappa}}\tag{9}$$

To further simplify the energy equation, the enthalpy and internal energy were written in terms of specific heat capacities, and these were assumed not to change much incrementally. This gave

$$\begin{aligned}&\varphi\frac{\partial}{\partial t}\left(X^{\kappa}T+\frac{(1-\varphi)\rho_R c_R}{\varphi\rho^{\kappa}c_V^{\kappa}}T\right)\\&=-\frac{d}{dy}\left(\frac{kX^{\kappa}c_p^{\kappa}T}{\mu^{\kappa}c_V^{\kappa}}\frac{dp}{dy}\right)-\frac{\lambda}{\rho^{\kappa}c_V^{\kappa}}\nabla^2 T+\frac{w^{\kappa}}{\rho^{\kappa}}\end{aligned}\tag{10}$$

The thermal diffusion coefficient, $\lambda/c_V^{\kappa}\rho^{\kappa}$, was on the order of 10^{-3} m^2/s. Also the quantity

$$v=-\frac{k}{\mu}\frac{dp}{dy}\tag{11}$$

is the Darcy velocity. In many of the single fracture studies this velocity remained approximately constant (at around 10^{-3} m/s). Therefore equations (9) and (10) would further simplify to

$$\varphi\frac{\partial}{\partial t}(X^{\kappa})=v\frac{d}{dy}\left(X^{\kappa}\right)+\frac{q^{\kappa}}{\rho^{\kappa}}\tag{12}$$

and

$$\begin{aligned}&\varphi\frac{\partial}{\partial t}\left(X^{\kappa}T+\frac{(1-\varphi)\rho_R c_R}{\varphi\rho^{\kappa}c_V^{\kappa}}T\right)\\&=-v\frac{d}{dy}\left(\frac{c_p^{\kappa}}{c_V^{\kappa}}X^{\kappa}T\right)-\frac{\lambda}{\rho^{\kappa}c_V^{\kappa}}\nabla^2 T+\frac{w^{\kappa}}{\rho^{\kappa}}\end{aligned}\tag{13}$$

The flow velocity was generally on the order of 10^{-3} m/s and the ratio of specific heat capacities was close to one.

Some further simplifications may be possible e.g. by placing the source/sink terms in the boundary conditions but in any case, this coupled system of partial differential equations remains complex – i.e. and ideal candidate for solution via numerical simulation.

STUDY OF A SINGLE FRACTURE

The first study undertaken was that of a single fracture. For the base case the fracture had 1 mm aperture, and length and height equal to 1 m. Water with temperature 100 C was injected on one end of the fracture and produced on the other. The flow velocity was kept constant at 1 mm/sec and the reservoir had an initial temperature of 200 C. To limit numerical dispersion the computational grid was set up such that the fracture was broken into 100, equally long segments (Figure 4). The boundaries were modeled as closed to both mass and heat transfer, at a distance of 0.5 m from the fracture walls, and the matrix had zero permeability.

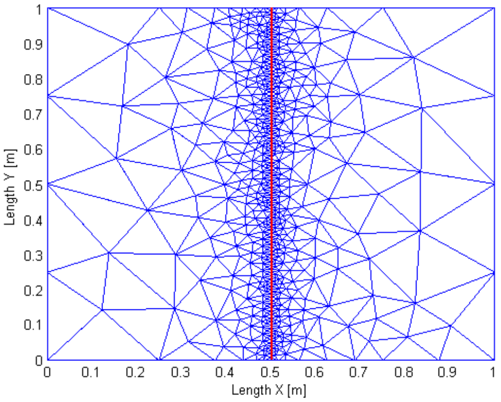

Figure 4: Computational grid for a single fracture, broken lengthwise into 100 segments.

The time step was limited to 200 seconds, for the first day of simulation. This way the estimated numerical dispersion (eq. (14), Lange, Bousian, & B. Bourbiaux, (2005)) would be similar to the estimated Taylor dispersion (eq. (15), Horne & Rodriguez, (1983))

$$D_{num}^{imp.sat.} = \frac{v\Delta x}{2} + \frac{v^2 \Delta t}{2} \qquad (14)$$

$$D_{Taylor} \approx \frac{2}{105} \frac{v^2 b^2}{d_{mol}} \qquad (15)$$

Here v is flow velocity, and Δx and Δt are gridblock length and time step size, respectively, b is fracture aperture and d_{mol} is molecular diffusivity which is usually on the order of 10^{-10}m^2/s for tracers in liquid water. Note that the time step term in eq. (14) dominates.

Figure 5 shows the normalized temperature and tracer returns on a logarithmic time scale.

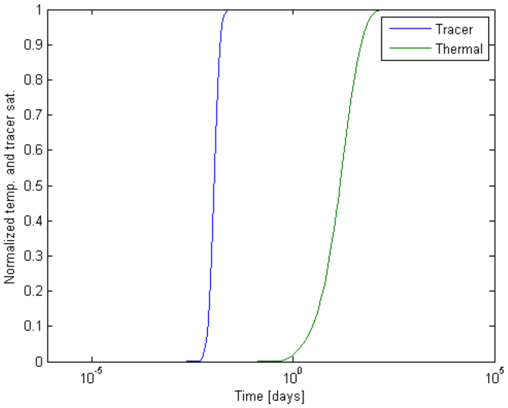

Figure 5: Normalized temperature and tracer returns for the base case.

The estimated arrival time was calculated as the point at which the return profiles reached the value 0.5. For the tracer this yielded $t_{tr,0.5} = \bar{t}_{tr} = 0.0107$ days, and for the temperature $t_{T,0.5} = \bar{t}_T = 14.6$ days.

The dispersion coefficient was calculated using the formulation (Bear, 1972)

$$D = \frac{1}{8}\left(\frac{t_{0.841} - t_{0.159}}{t_{0.5}}\right)^2 \frac{L^2}{t_{0.5}\varphi} \qquad (16)$$

where L is the fracture length. In this case the tracer dispersion was $D_{tr} = 4.6\times10^{-5}$ m^2/s which was actually a bit less than predicted from eq. (14) because the simulator automatically reduced the time step well below 200 sec during several of the first iterations. The dispersion coefficient for the temperature return was $D_T = 5.97\times10^{-7}$ m^2/s.

Several variations of the base case were studied to gain understanding of the sensitivity of the return profiles to various factors

Varying Fracture Aperture

The first study undertaken was to vary the fracture aperture in the model. Note that the flow velocity was kept constant (as opposed to the injection rate). The aperture was given the values $b = \{0.1, 0.3, 1, 3, 10\}$ mm.

The tracer return profiles remained effectively the same for all cases, as expected since Taylor dispersion (eq. (15)) was not part of the simulation code. The thermal return curves however, varied considerably. In particular the mean thermal return times seemed to follow a trend where (see Figure 6)

$$\overline{t}_T \propto \frac{1}{b^n} \tag{17}$$

and n varied from approximately 1 for smaller apertures to around 2 as the aperture was made larger.

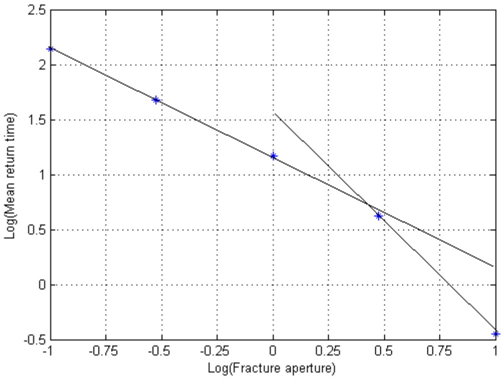

Figure 6: Logarithm of thermal front return time as a function of the logarithm of fracture aperture. The two illustrative lines have slope -1 and -2.

A similar trend was seen in the dispersion coefficient for the thermal return profile (Figure 7), i.e.

$$D_T = b^m \tag{18}$$

where m seems to vary from around 1 to 4 as the fracture aperture gets larger.

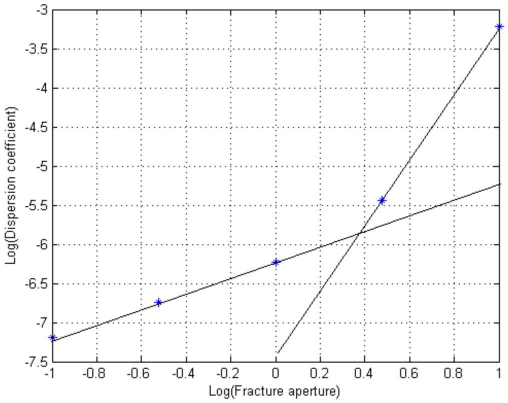

Figure 7: Logarithm of thermal front dispersion coefficient as a function of the logarithm of fracture aperture. The two illustrative lines have slope ~1 and ~4.2.

Although the models postulated here do not explain the variation in return times very accurately it is clear that both the thermal return time and dispersion are highly dependent on the fracture aperture. This is because flow velocity is kept constant and therefore the total flow rate through the fracture varies linearly with the aperture. This corresponds directly to the temperature decline for small apertures (flow rates) while for larger apertures (flow rates) the thermal decline becomes more rapid. The deviation from linearity is likely caused by interaction with the boundary although an explicit formulation for the boundary condition interaction was not found.

Varying Boundary Distance

The second parameter investigated was the distance from the fracture to the side boundaries, i.e. the length of the x-axis on Figure 4. The distance was varied from 0.25 to 50 m.

Again, the tracer front stayed more or less the same in all cases but the thermal front varied. As seen in Figure 8, the thermal return time varied approximately as the square root of the boundary distance when the distance was small (0.25 to 2.5 meters). When the boundary distance got larger however, the thermal return time stopped increasing, because the size of the reservoir became “infinite acting”, i.e. it was as if there was an open boundary.

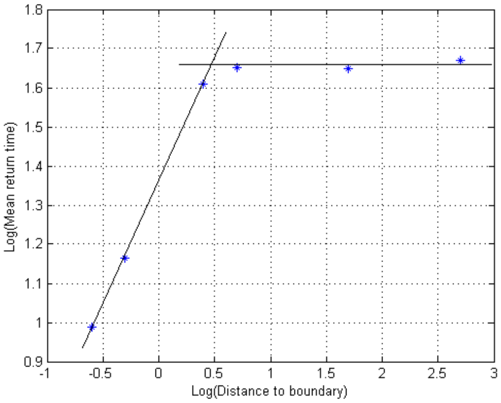

Figure 8: Logarithm of thermal front return time as a function of the logarithm of distance to the reservoir boundary. The two illustrative lines have slope ~0.5 and 0.

The thermal dispersion coefficient also ranged by a factor of about 10 in the various different cases, as can be seen in Figure 9. The trend in this case was not clear although one may propose that the three smallest distances are dominated by closed boundary effects, while the fourth is an intermediate case, and the two largest distances are representative of an open boundary.

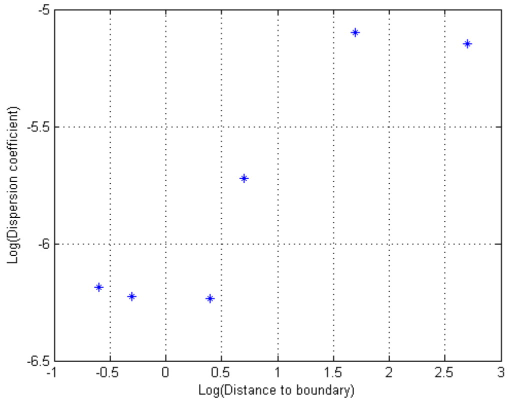

Figure 9: Logarithm of thermal front dispersion coefficient as a function of the logarithm of distance to the reservoir boundary.

Varying Flow Velocity

The effects of varying flow velocity were also studied. The flow velocity was varied in a similar way to the fracture aperture, i.e. $v = \{0.1, 0.3, 1, 3, 10\}$ mm/s. Here both the thermal and tracer return profiles varied from case to case. Of course the mean tracer return time was inversely proportional to the flow velocity. Moreover, the tracer dispersion coefficient increased with a close to linear relation to the flow velocity as seen in Figure 10.

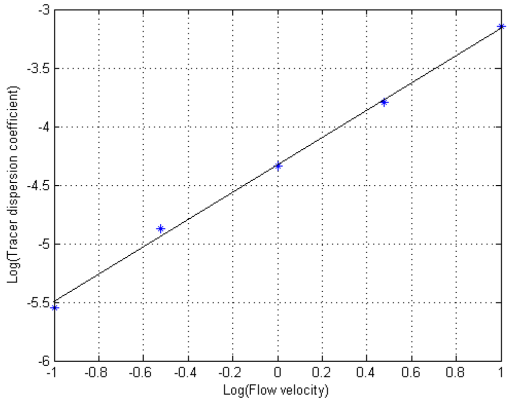

Figure 10: Logarithm of tracer front dispersion coefficient as a function of the logarithm of flow velocity. The illustrative line has slope ~1.2.

In fact the slope of the best line through the points in Figure 10 was around 1.2, that is

$$D_{tr} \propto v^{1.2} \tag{19}$$

which was not entirely in line with the expected value from equation (14).The deviation could have been caused by the GPRS simulator automatically reducing the time step.

The thermal arrival time and dispersion coefficient behaved very similarly to the way they did in the varying aperture case as shown in Figure 11 and Figure 12.

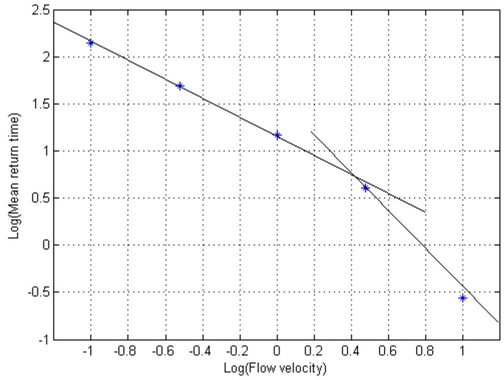

Figure 11: Logarithm of thermal front return time as a function of the logarithm of fracture flow velocity. The two illustrative lines have slope -1 and -2.

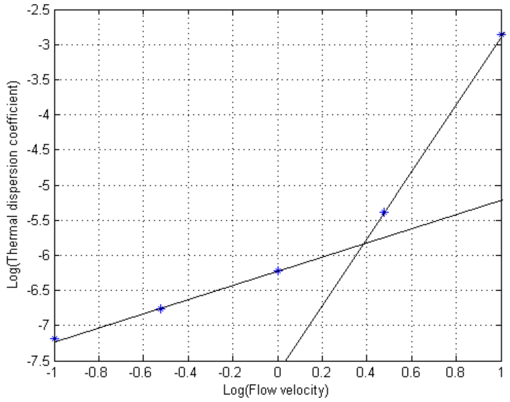

Figure 12: Logarithm of thermal front dispersion coefficient as a function of the logarithm of fracture flow velocity. The two illustrative lines have slope ~1 and ~4.6.

The reason for this similarity between the thermal behavior for the varying aperture and varying velocity case is that the total injection rate is the same in all corresponding cases. Therefore, one might say that the thermal return profile is very sensitive to the flow rate through the fracture, rather than the velocity or the aperture. These three quantities are of course all related through Darcys law

$$\begin{aligned} Q &= bHv(b) = bH\frac{k(b)}{\mu}\frac{dp}{dy} \\ &= H\frac{b^3}{24\mu}\frac{dp}{dy} \end{aligned} \tag{20}$$

Here Q is the volumetric flow rate H is the fracture height and all other quantities as defined earlier.

Other cases

A few other cases were studied in addition to those above. For example, varying the injection temperature had almost no effect on the return profiles. Increasing the matrix permeability up to 100 md also had very little effect.

Modeling an open boundary by giving the edge blocks (at 0.5 m lateral distance) a very large volume was also considered. This lead to very little changes in the tracer profile but the thermal return changed in the sense that the cold water never fully broke through; in stead it came to a balance temperature of around 120 C.

STUDY OF MULTIPLY FRACTURED RESERVOIR

Observations for a single fracture seemed to suggest that the thermal return curves were highly dependent on the flow rate through the fracture and the distance to the matrix boundary. The distance to the boundary can in a sense be understood as the fracture density. Therefore we ran two cases, one with a sparsely fractured reservoir and another where a large number of smaller fractures had been added. The aperture of the fractures varied in linear relation to the fracture lengths, such that they spanned a range of about 0.1 to 10 mm. The size of the reservoir was also set to 100x100x100 meters and the matrix was given permeability 1 md. The injection rate was fixed at 10 kg/s. The sparse and dense fracture networks (with around 40 and 300 fractures, respectively) are shown in Figure 13.

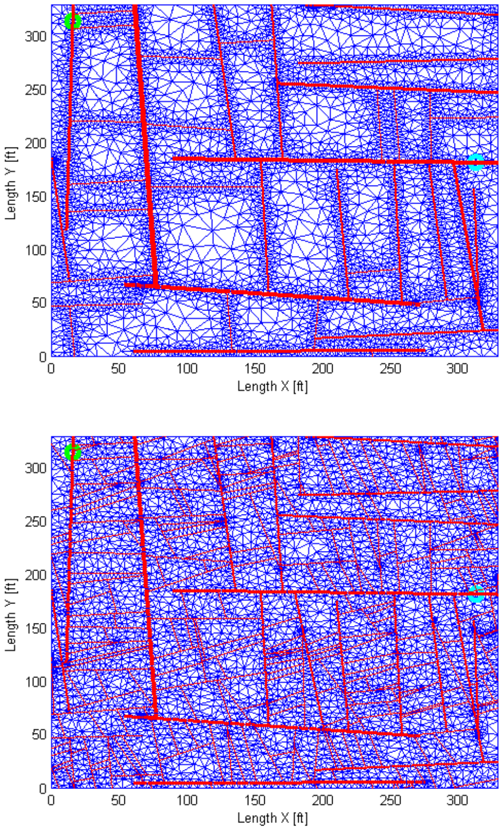

Figure 13: Sparse network of 40 fractures (above) and dense network of 300 fractures (below). The injector and producer are denoted by green and cyan circles, respectively. The width of the fracture lines (red) is indicative of the aperture.

Spatial Property Propagation

The propagation of pressure, temperature and tracer could be visualized and compared for the two cases. The following figures are snapshots of these property distributions after 12 hours of injection.

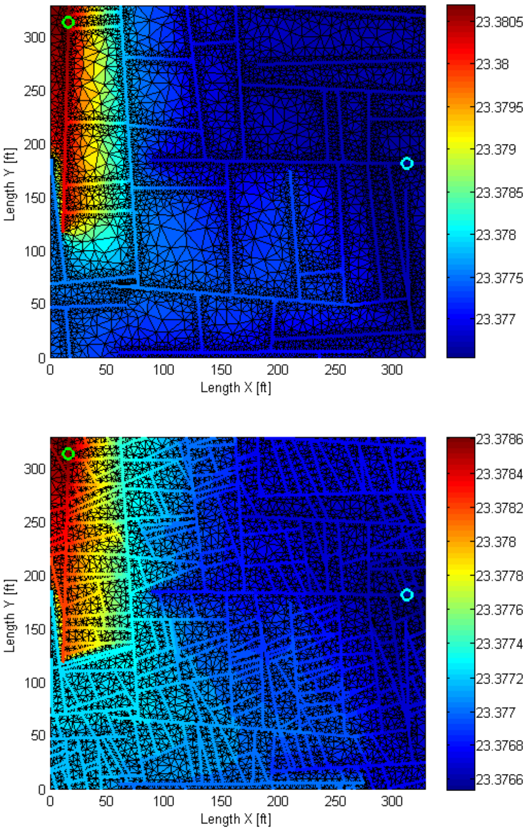

Figure 14: Pressure distribution after 12 hours of injection for the two fracture networks studied.

As Figure 14 shows, the pressure propagated in a diffusive nature as expected due to the elliptical character of the pressure equation. The pressure gradient spread considerably into the matrix in both cases, but in the denser network the pressure change spread further into the reservoir.

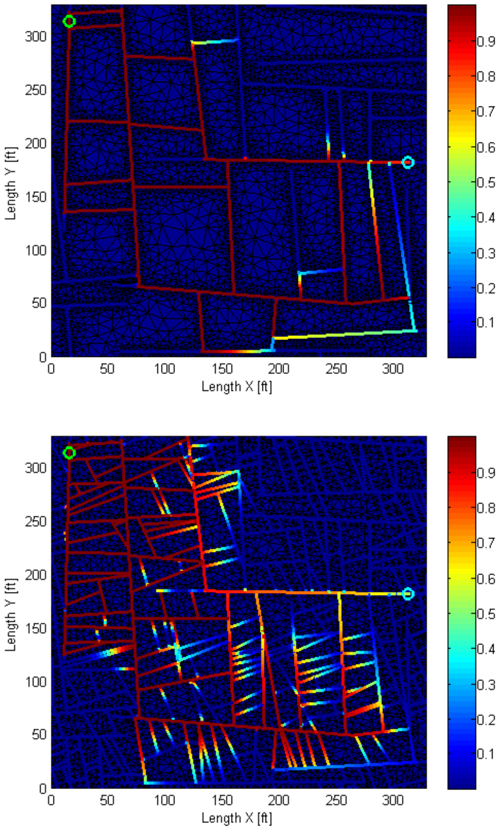

Figure 15: Tracer distribution after 12 hours of injection for the two fracture networks studied.

The tracer distribution in the reservoir is shown in Figure 15. The tracer propagation was dominated by convection (in fact diffusion effects were not modeled so the dispersion seen in the fractures is all numerical) and therefore the tracer flowed almost exclusively through the fractures. The flow through the denser network is clearly much more dispersive, which indicates that more effective heat extraction would be achievable.

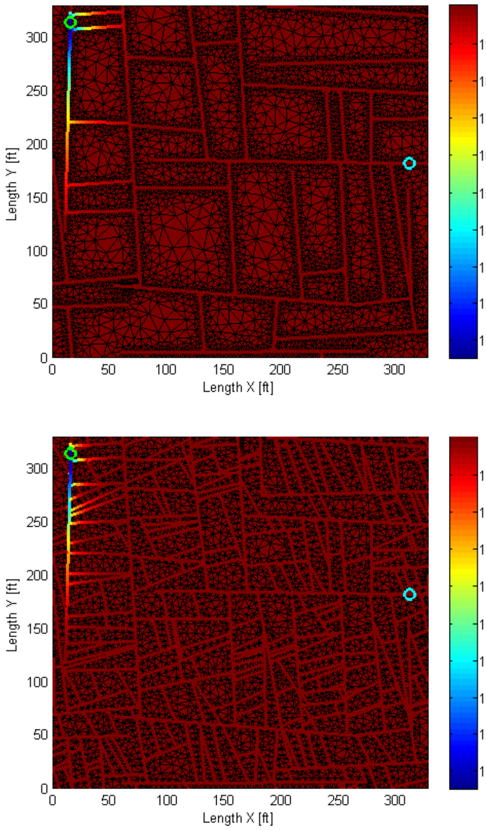

Figure 16: Thermal distribution after 12 hours of injection for the two fracture networks studied.

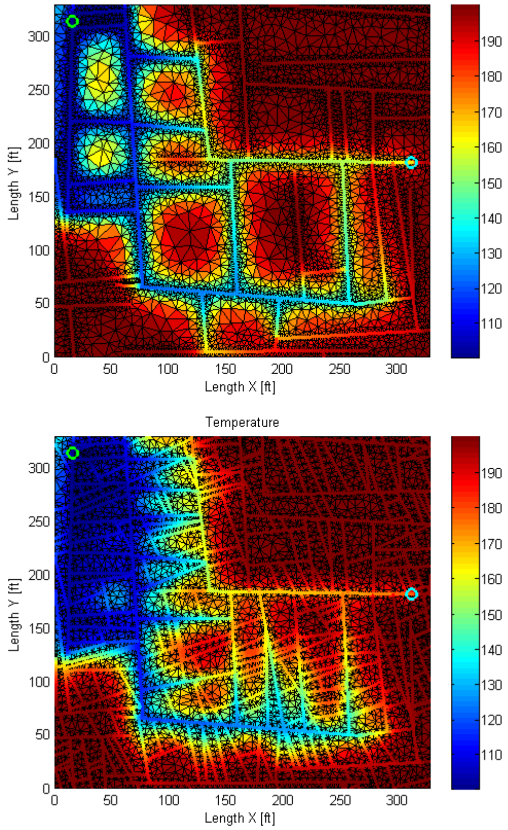

Figure 17: Thermal distribution after approx. 280 days of injection for the two fracture networks studied.

Figure 16 illustrates the temperature distribution after 12 hours of injection. At this time the thermal front seemed to be traveling mostly through the fractures. However, the front would not propagate much unless the surrounding matrix blocks had started cooling. This is perhaps better seen in Figure 17 which illustrates the thermal distribution after 280 days. Therefore one might say the thermal front traveled in a mixed convective/diffusive manner.

Return Profile Comparison

The main characteristics of the return profiles for the two simulation scenarios were computed in a manner similar to that for the single fracture cases. The results are summarized in Table 2.

Table 2: Characteristics of return profiles for the two simulation cases studied. Time is in days, dispersion is in m^2/sec

	$\bar{t}_{tr}$	D_{tr}	$\bar{t}_T$	D_T
Sparse	0.30	$4.8\text{x}10^{-2}$	425	$3.1\text{x}10^{-4}$
Dense	0.47	$6.1\text{x}10^{-2}$	546	$1.0\text{x}10^{-4}$

Then denser network gave a longer mean return time for both the tracer and temperature. The change in the dispersion coefficient was however small, and for the temperature the dispersion coefficient was lower in the dense fracture network case. For the tracer this indicated that the density of the fracture network did not have as much effect on the dispersion coefficient as did numerical dispersion (or physically, Taylor dispersion, which would be similar to in magnitude to the numerical dispersion). The fact that the thermal dispersion coefficient was smaller for the dense fracture network indicated that a more uniform front swept the reservoir.

The corresponding return curves from each of the simulation cases were compared on a quantile plot. This plot compares the times at which a certain quantile of the injection value is obtained on the production side. In Figure 18 the quantiles for the tracer return curves are compared. The fact that the quantile values all fell on the left of the 45 degree line meant that the tracer return time tended to be larger for the dense fracture case, and this difference got larger at later times.

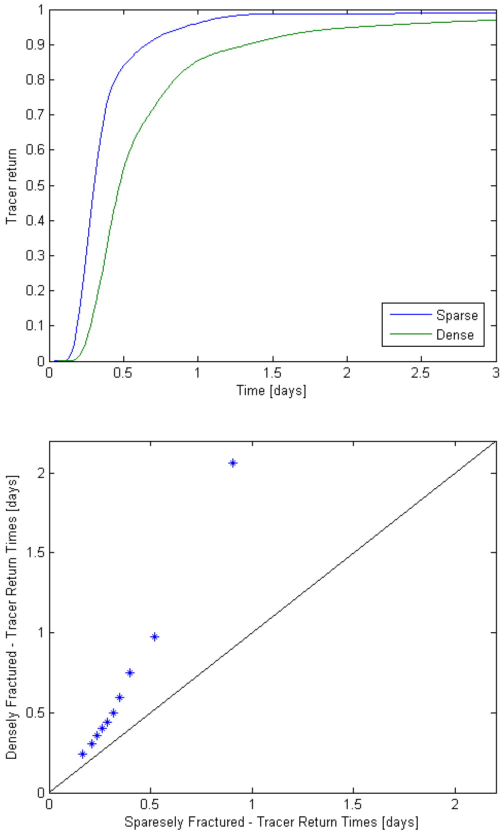

Figure 18: Comparison of the tracer return profiles for the sparse and dense fracture networks. The graph above is the derivative of the return profile. The graph below is a quantile plot comparing the two return distributions.

Figure 19 compares the two temperature return curves. These two return curves were clearly much more similar which was well conveyed on the quantile plot. For the dense fracture case the initial return quantiles were larger than those for the sparse case, but at later times the trend reversed. This pointed to a better thermal sweep in the dense fracture case. In other words, residual thermal energy was being swept from the reservoir for a slightly longer time in the sparse fracture case, and the bulk of the cooling came earlier.

As a final note of interest we mention that the tracer return profiles showed some “large scale” changes in the slope (Figure 18), which we believed to be strongly related to the fracture distribution. The thermal return showed more smooth variations (Figure 19) because of the strong thermal interaction with the matrix blocks.

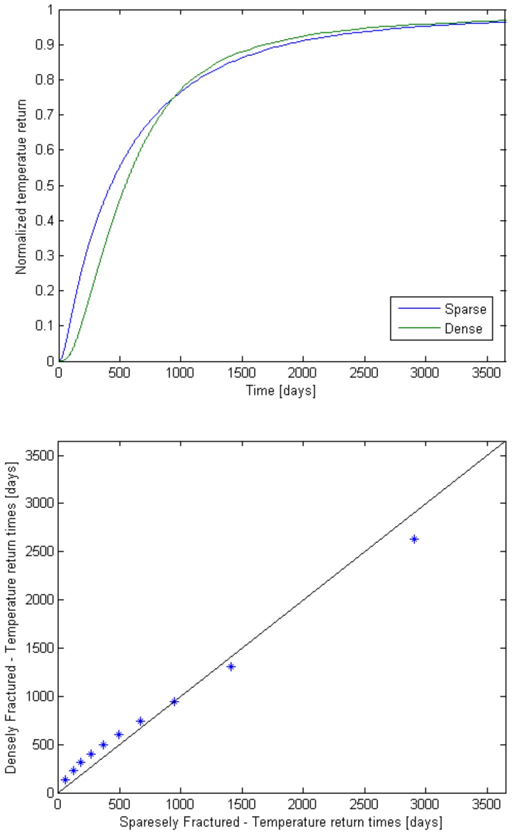

Figure 19: Comparison of the normalized temperature return profiles for the sparse and dense fracture networks. The graph above is the derivative of the return profile. The graph below is a quantile plot comparing the two return distributions.

CONCLUSIONS

The combined transport of tracer and temperature through a fracture network was studied through a number of simulations. The simulations were based on an efficient fracture discretization scheme developed by Karimi-Fard et al. (2003). The simulation code used was the General Purpose Research Simulator (GPRS) developed at the Department of Energy Resources Engineering at Stanford University.

The simulations on a single fracture showed that the thermal return profile is very sensitive to the extent of the matrix surrounding the fracture and the flow rate through the fracture.

Simulations on two fracture networks of varying fracture density indicated that the tracer return profile was more sensitive to the fracture density and/or connectivity, than was the thermal return profile. The thermal return profile did not vary as much since it was very much affected by bulk interaction with the matrix.

Some suggestions for future work of interest might be to try using an appropriate upscaling algorithm (e.g. Gong, 2007) and compare the results obtained to the method used here. This would be useful since the computational time for the dense fracture network was on the margin of being feasible. Another way to make these computations more efficient might be use a total variation diminishing scheme (Lange, Bousian, & B. Bourbiaux, (2005) Wu & Forsyth, (2008)). Moreover, it seems like adding a formulation of Taylor dispersion should be possible if the explicit fracture discretization of Karimi-Fard et al. (2003) is used.

Finally a more thorough analysis of the governing equations and the statistical relationship between fracture distributions and the return distributions would be of interest, although that seems to be a non-trivial task.

ACKNOWLEDGEMENTS

This research was conducted with financial support to the Stanford Geothermal Program from the US Department of Energy under grant DE-FG36-08GO18192, the contribution of which is gratefully acknowledged.

REFERENCES

Bear, J. (1972), “Dynamics of fluids in porous media,” *Dover*, pp. 1-764,.

Bodvarsson, G., & Pruess, K. (1984), “Thermal effects of reinjection in geothermal reservoirs with major vertical fractures,” *Journal of Petroleum Technology*, **36**, 1567–1578.

Cao, H. (2002), “Development of techniques for general purpose simulators,” Ph.D. Thesis, Stanford University.

Gong, B. (2007), “Effective models of fractured systems,” Ph.D Thesis, Stanford University

Horne, R., & Rodriguez, F. (1983), “Dispersion in tracer flow in fractured geothermal systems,” *Proceedings of Seventh Workshop on Geothermal Reservoir Engineering*, 103-107.

Horne, R., & Szucs, P. (2007), “Inferring Well-to-Well Connectivity Using Nonparametric Regression on Well Histories,” *Proceedings of Thirty-Second Workshop on Geothermal Reservoir Engineering*.

Juliusson E. and Horne, R.N. (2009), “Fracture characterization using production and injection data,” *DOE quarterly report (2009 January to March), Contract DE-FG36-08GO18192*, 1-17.

Karimi-Fard, M., Durlofsky, L. & Aziz, K. (2003), “An Efficient Discrete Fracture Model Applicable for General Purpose Reservoir Simulators,” *Proceedings of SPE Reservoir Simulation Symposium*, 1-11.

Lange, A., Bousian, J. & B. Bourbiaux. (2005), “Tracer-Test Simulation on Discrete Fracture Network Models for the Characterization of Fractured Reservoirs,” *SPE Europec/EAGE Annual Conference,* 1-10.

Lovekin, J. & Horne, R. (1989), “Optimization of injection scheduling in geothermal fields. Conference,” *Proceedings of the Geothermal Program Review VII*, 45-52.

Shewchuk, J. (1996), “Triangle: Engineering a 2D quality mesh generator and Delaunay triangulator,” *Lecture Notes in Computer Science*, **1148**, 203–222.

Sullera, M., & Horne, R. (2001), “Inferring injection returns from chloride monitoring data,” *Geothermics*, **30**, 591–616.

Urbino, E. G., & Horne, R. (1991), “Optimizing reinjection strategy at Palinpinon, Philippines, based on chloride data,” *Proceedings of Sixteenth Workshop on Geothermal Reservoir Engineering*.

Voskov, D. (2006), “Description of the Thermal GPRS,” Technical Report, Department of Energy Resources Engineering, Stanford University.

Wu, Y. (2000), “Numerical simulation of non-isothermal multiphase tracer transport in heterogeneous fractured porous media” *Advances in Water Resources*, **23**, 699-723.

Wu, Y. & Forsyth, P.a. (2008), “Efficient Schemes for Reducing Numerical Dispersion in Modeling Multiphase Transport through Heterogeneous Geological Media” *Vadose Zone Journal*, **7**, 340-349.